Double-charm and hidden-charm hexaquark states under the complex scaling method

Jian-Bo Cheng,[1,*] Du-xin Zheng,[2,†] Zi-Yang Lin,[1,‡] and Shi-Lin Zhu[1,§]

[1]*School of Physics and Center of High Energy Physics, Peking University, Beijing 100871, China*
[2]*Shandong Institute of Advanced Technology, Jinan 250100, China*

(Received 11 November 2022; accepted 20 February 2023; published 13 March 2023)

We investigate the double-charm and hidden-charm hexaquarks as molecules in the framework of the one-boson-exchange potential model. The multichannel coupling and $S-D$ wave mixing are taken into account carefully. We adopt the complex scaling method to investigate the possible quasibound states, whose widths are from the three-body decay channel $\Lambda_c\Lambda_c\pi$ or $\Lambda_c\bar{\Lambda}_c\pi$. For the double-charm system of $I(J^P)=1(1^+)$, we obtain a quasibound state, whose width is 0.50 MeV if the binding energy is -14.27 MeV, and the S-wave $\Lambda_c\Sigma_c$ and $\Lambda_c\Sigma_c^*$ components give the dominant contributions. For the $1(0^+)$ double-charm hexaquark system, we do not find a pole. We find more poles in the hidden-charm hexaquark system. We obtain one pole as a quasibound state in the $I^G(J^{PC})=1^+(0^{--})$ system, which only has one channel $(\Lambda_c\bar{\Sigma}_c+\Sigma_c\bar{\Lambda}_c)/\sqrt{2}$. Its width is 1.72 MeV with a binding energy of -5.37 MeV, but we do not find a pole for the scalar $1^-(0^{-+})$ system. For the vector $1^-(1^{-+})$ system, we find a quasibound state. Its energies, widths, and constituents are very similar to those of the $1(1^+)$ double-charm case. In the vector $1^+(1^{--})$ system, we get two poles—a quasibound state and a resonance. The quasibound state has a width of 0.38 MeV with a binding energy of -16.79 MeV. For the resonance, its width is 4.06 MeV with an energy of 60.78 MeV relative to the $\Lambda_c\bar{\Sigma}_c$ threshold, and its partial width from the two-body decay channel $(\Lambda_c\bar{\Sigma}_c-\Sigma_c\bar{\Lambda}_c)/\sqrt{2}$ is apparently larger than the partial width from the three-body decay channel $\Lambda_c\bar{\Lambda}_c\pi$. In particular, the $1^+(0^{--})$ and $1^-(1^{-+})$ hidden-charm hexaquark molecular states are very interesting. These isovector mesons have exotic J^{PC} quantum numbers which are not accessible to the conventional $q\bar{q}$ mesons.

DOI: 10.1103/PhysRevD.107.054018

I. INTRODUCTION

In the study of the hadronic molecular states, the dibaryon always plays an important role. The well-known deuteron is the only experimentally confirmed baryon-baryon bound state without charm quarks. Moreover, the WASA-at-COSY Collaboration repeatedly observed the dibaryon resonance $d^*(2380)$ [1–5]. It is natural to extend the investigation from the deuteron to the strange dibaryon. Jaffe suggested the famous H-dibaryon composed of the $\Lambda\Lambda$ pair [6], which was also studied in a series of works [7–19]. In addition, the dibaryon with one heavy quark ($qqqqQ$) was also investigated in Refs. [20–22].

In 2017, the LHCb Collaboration discovered a double-charm baryon in the $\Lambda_c^+K^-\pi^+\pi^-$ mass spectrum Ξ_{cc}^{++} [23], which is also the first observed double-heavy hadron. This discovery encouraged the research on the double-heavy hadrons, especially the double-charm tetraquarks [24–33]. After four years, the LHCb Collaboration reported the observation of the first double-heavy exotic hadron T_{cc}^+ [34,35]. After the rapid succession of the double-charm hadron discovery, it is necessary to implement a further investigation. We will focus on the double-charm deuteron-like hexaquarks in this work.

In the molecule picture, the double-charm dibaryon could be easier to form a bound state due to the larger reduced mass. And in fact, the double-heavy hexaquark ($qqqqQQ$) systems have been discussed in various approaches [36–53], including the chiral constituent quark model [36,37], the quark delocalization color screening model [38,39], the chromomagnetic model [40], the QCD sum rules [41], the chiral effective field theory [42,43], and the one-boson-exchange (OBE) model [44–50]. For the $\Lambda_c\Sigma_c$ molecule system, the authors of Ref. [46] found a bound state with the number $I(J^P)=1(1^+)$. However, it

*jbcheng@pku.edu.cn
†duxin.zheng@iat.cn
‡lzy_15@pku.edu.cn
§zhusl@pku.edu.cn

was not confirmed in Ref. [39]. The hidden-heavy hexaquark $(qqQ\bar{q}\,\bar{q}\,\bar{Q})$ may have similar behaviors, and the relevant investigations can be found in Refs. [54–60].

In this work, we investigate the double-charm dibaryon and hidden-charm baryonium systems containing the $\Lambda_c\Sigma_c^{(*)}$ and $\Lambda_c\bar{\Sigma}_c^{(*)}$ channels in the molecule picture. As pointed out in our previous works [61,62], the cross diagram $DD^* \leftrightarrow D^*D$ of the one-pion exchange will provide a complex potential, which is from the three-body decay effect. This behavior could also occur in the process $\Lambda_c\Sigma_c^{(*)} \leftrightarrow \Sigma_c^{(*)}\Lambda_c$. To study the possible three-body effect, we will retain the imaginary contribution from the one-pion exchange (OPE) potential.

We use the OBE model to deal with the molecule state system. In order to explore the existence of the resonance, we will adopt the complex scaling method (CSM) [63,64], which is a powerful method that can handle the bound state and resonance in a consistent way. In addition, the $S-D$ wave mixing and coupled-channel effect will be considered in this work. For both the double-charm and hidden-charm hexaquarks, the dominant contributions of the widths arise from the open-charm decay processes. The possible hidden-charm decay contributions for the hidden-charm hexaquark systems are negligible.

This paper is organized as follows. In Sec. II, we introduce our framework explicitly. In Sec. III, we present the effective Lagrangians and potentials. In Sec. IV, we solve the complex scaled Schrödinger equation and give the results of the double-charm dibaryon and hidden-charm baryonium. The last section, Sec. V, is a brief summary.

II. FRAMEWORK

In previous works [61,62], we studied the double-charm tetraquark with the CSM method. The DD^* system is found to be special since the zeroth component of the transferred momentum of the exchanged pion is larger than the pion mass. This feature will provide the OPE potential with an imaginary part. If one could get a pole in this system, one may get an energy with an imaginary part which is explained as its half-width. Therefore, we will pay more attention to the systems containing this type of interaction. One could see similar interactions in several systems, such as $\Lambda_c\Sigma_c \leftrightarrow \Sigma_c\Lambda_c$, $\Lambda_c\bar{\Sigma}_c \leftrightarrow \Sigma_c\bar{\Lambda}_c$, $\Lambda_cD^* \leftrightarrow \Sigma_cD$ and $\Lambda_c\bar{D}^* \leftrightarrow \Sigma_c\bar{D}$. In this work, we consider the former two cases: the double-charm and hidden-charm hexaquark molecule system.

To find the possible bound and resonant states, we take into account the coupled-channel effect. The explicit systems and channels can be seen in Table I. However, we do not consider the isoscalar system with channels $\Lambda_c\Lambda_c$, $\Sigma_c\Sigma_c$, and $\Sigma_c^*\Sigma_c^*$ (or $\Lambda_c\bar{\Lambda}_c$, $\Sigma_c\bar{\Sigma}_c$, and $\Sigma_c^*\bar{\Sigma}_c^*$) in this work. Unlike the other two isovector systems, this system does not have the special cross diagram and could not contribute an imaginary part to the OPE potential. We will study these systems in subsequent work. For the isovector cases, we will not take into account channels $\Sigma_c\Sigma_c^*$ and $\Sigma_c^*\Sigma_c^*$ (or $\Sigma_c\bar{\Sigma}_c^*$ and $\Sigma_c^*\bar{\Sigma}_c^*$) due to the same reason. In this work, we only consider the channels with $^1S_0$ $(J=0)$, $^3S_1$ $(J=1)$, and $^3D_1$ $(J=1)$.

The masses of the charmed baryon and exchanged light mesons are shown in Table II. We take the isospin mean masses to deal with the isospin conservation process.

A. A brief discussion on the CSM

We first briefly introduce the CSM before investigating the analyticity of the OPE potentials. Aguilar, Balslev, and Combes proposed this method in the 1970s [63,64], and the corresponding conclusion is known as the ABC theorem. In this powerful method, the resonances can be solved in the same way as the bound states. The transformation of the radial coordinate r and its conjugate momentum k in the CSM is defined by

$$U(\theta)r = re^{i\theta}, \qquad U(\theta)k = ke^{-i\theta}. \tag{1}$$

Then, the radial Schrödinger equation is transformed as

TABLE I. The channels of the double- and hidden-charm hexaquark systems. We adopt the following shorthand notations for simplicity: $[\Lambda_c\bar{\Sigma}_c^{(*)}] = \frac{1}{\sqrt{2}}(\Lambda_c\bar{\Sigma}_c^{(*)} - \Sigma_c^{(*)}\bar{\Lambda}_c)$ and $\{\Lambda_c\bar{\Sigma}_c^{(*)}\} = \frac{1}{\sqrt{2}}(\Lambda_c\bar{\Sigma}_c^{(*)} + \Sigma_c^{(*)}\bar{\Lambda}_c)$.

	$I^G(J^{PC})$	1	2	3	4	5	6
cc	$0(0^+)$	$\Lambda_c\Lambda_c(^1S_0)$	$\Sigma_c\Sigma_c(^1S_0)$	$\Sigma_c^*\Sigma_c^*(^1S_0)$			
	$1(0^+)$	$\Lambda_c\Sigma_c(^1S_0)$					
	$1(1^+)$	$\Lambda_c\Sigma_c(^3S_1)$	$\Lambda_c\Sigma_c(^3D_1)$	$\Lambda_c\Sigma_c^*(^3S_1)$	$\Lambda_c\Sigma_c^*(^3D_1)$	$\Sigma_c\Sigma_c(^3S_1)$	$\Sigma_c\Sigma_c(^3D_1)$
$c\bar{c}$	$0^+(0^{-+})$	$\Lambda_c\bar{\Lambda}_c(^1S_0)$	$\Sigma_c\bar{\Sigma}_c(^1S_0)$	$\Sigma_c^*\bar{\Sigma}_c^*(^1S_0)$			
	$1^+(0^{--})$	$\{\Lambda_c\bar{\Sigma}_c\}(^1S_0)$					
	$1^-(0^{-+})$	$[\Lambda_c\bar{\Sigma}_c](^1S_0)$	$\Sigma_c\bar{\Sigma}_c(^1S_0)$				
	$1^+(1^{--})$	$[\Lambda_c\bar{\Sigma}_c](^3S_1)$	$[\Lambda_c\bar{\Sigma}_c](^3D_1)$	$\{\Lambda_c\bar{\Sigma}_c^*\}(^3S_1)$	$\{\Lambda_c\bar{\Sigma}_c^*\}(^3D_1)$	$\Sigma_c\bar{\Sigma}_c(^3S_1)$	$\Sigma_c\bar{\Sigma}_c(^3D_1)$
	$1^-(1^{-+})$	$\{\Lambda_c\bar{\Sigma}_c\}(^3S_1)$	$\{\Lambda_c\bar{\Sigma}_c\}(^3D_1)$	$[\Lambda_c\bar{\Sigma}_c^*](^3S_1)$	$[\Lambda_c\bar{\Sigma}_c^*](^3D_1)$		

TABLE II. The masses of the charmed baryons and exchanged light mesons in the OBE potential, which are taken from the Particle Data Group [65].

Mesons	Mass (MeV)	Mesons	Mass (MeV)
Λ_c^+	2286.46	σ	600
Σ_c^{++}	2453.97	$\pi^\pm$	139.57
Σ_c^+	2452.65	π^0	134.98
Σ_c^0	2453.75	η	547.86
Σ_c^{*++}	2518.41	ρ	775.26
Σ_c^{*+}	2517.4	ω	782.66
Σ_c^{*0}	2518.48		

$$\left\{\frac{1}{2m}\left[-\frac{d^2}{dr^2}+\frac{l(l+1)}{r^2}\right]e^{-2i\theta}+V(re^{i\theta})\right\}\psi_l^\theta(r) = E(\theta)\psi_l^\theta(r). \tag{2}$$

After the complex scaling operation, the resonance pole will cross the branch cut into the first Riemann sheet if the rotation angle θ is large enough, as shown in Fig. 1. In this way, the wave functions of the resonances become square integrable, just like the normalizable bound states. The details can be seen in Refs. [66,67].

In previous work [61], we adopted the Gaussian expansion method (GEM) [68] to solve the tetraquark system, and our results agreed with the experimental data very well. However, when dealing with resonances, the GEM may not be applicable to some extreme situations. For example, if there is a pole located on the second Riemann sheet corresponding to one of the channels, we need to make a complex scaling to move this pole to the first Riemann sheet. And when this pole is too close to or below the threshold, the rotation angle $\theta \gtrsim \pi/4$, which is out of the limit of the Gaussian basis, so we adopt another function as the basis sets—the Laguerre functions of the form

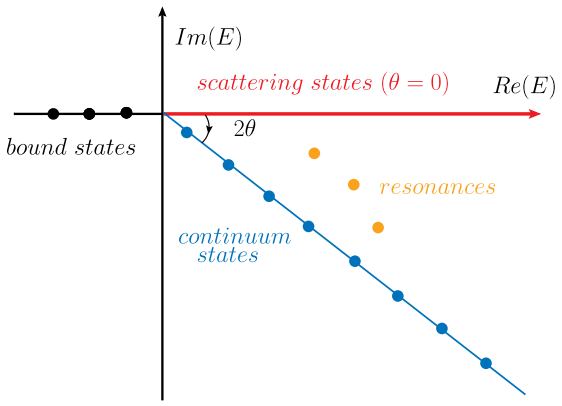

FIG. 1. The eigenvalue distribution of the complex scaled Schrödinger equation for two-body systems.

$$\phi_{nl}(\lambda r) = \sqrt{\frac{n!}{(2l+2+n)!}}(\lambda r)^{l+1}e^{-\lambda r/2}L_n^{2l+2}(\lambda r), \tag{3}$$

where λ is an adjustable parameter for the different size state. The radial wave function can be expanded as

$$\psi_l^\theta(r) = \sum_n^N c_n(\theta)\phi_{nl}(\lambda r), \tag{4}$$

where $c_n(\theta)$ is the rotation angle θ-dependent coefficient. These basis sets have some good characteristics: (1) We can get all the resonances located on the second Riemann sheets since the angle region becomes $0 < \theta < \pi/2$. (2) The basis functions are orthonormal. (3) One can evaluate all the Hamiltonian matrix elements with simple analytical formulas in the OBE potential case. (4) These basis sets can allow the wave function to have the oscillating behavior of trigonometric function in a infinite range so that one can get the partial width of the corresponding resonance with the golden rule [69,70]. One can find the concrete application in Ref. [71].

B. Analyticity of the OPE potentials for the $\Lambda_c\Sigma_c^{(*)}$ system

When considering the process $\Lambda_c\Sigma_c \to \Sigma_c\Lambda_c$, one can get potentials as follows:

$$V_\pi \propto \frac{1}{2f_\pi^2}\frac{(\boldsymbol{\sigma}\cdot\boldsymbol{q})(\boldsymbol{\sigma}\cdot\boldsymbol{q})}{q^2-m_\pi^2}, \tag{5}$$

where $\boldsymbol{\sigma}$ is the Pauli matrix. q is the transferred momentum of the pion, and q_0 is its zeroth component. The denominator above gives $q^2 - m_\pi^2 = -(\boldsymbol{q}^2 - m_{\rm eff}^2)$, where the shorthand $m_{\rm eff} = \sqrt{q_0^2 - m_\pi^2}$ and $q_0 \approx m_{\Sigma_c} - m_{\Lambda_c} > m_\pi$. Obviously, the poles are located on the real transferred momentum axis. When making a Fourier transformation, we adopt the Feynman prescription to make the contour integral, and the OPE potential is proportional to $1/(\boldsymbol{p}^2 - m_{\rm eff}^2 - i\epsilon)$. It is obvious that the complex scaling operation will not change the analyticity of the OPE potential. Compared with the DD^* system, we have an additional channel $\Lambda_c\Sigma_c^*$ that could provide a similar potential. The processes $\Lambda_c\Sigma_c^* \to \Sigma_c^*\Lambda_c$ and $\Lambda_c\Sigma_c \to \Sigma_c^*\Lambda_c$ could contribute an imaginary part too. To discuss this type of process, we have a careful discussion on q_0 herein. Since $m_{\Sigma_c} - m_{\Lambda_c}$ and m_π are comparable, the effective mass $m_{\rm eff} \approx \sqrt{2m_\pi(m_{\Sigma_c} - m_{\Lambda_c} - m_\pi)}$ is small. Therefore, the small bound energy could also affect $m_{\rm eff}$. To deal with q_0 in the $\Lambda_c\Sigma_c^{(*)} \to \Sigma_c^{(*)}\Lambda_c$ process, we denote the total energy as E and assume the Λ_c to be on shell. Then, $q_0 = E - \sqrt{m_{\Lambda_c}^2 + \boldsymbol{p}^2} - \sqrt{m_{\Lambda_c}^2 + \boldsymbol{p}'^2}$, as illustrated in Fig. 2(a).

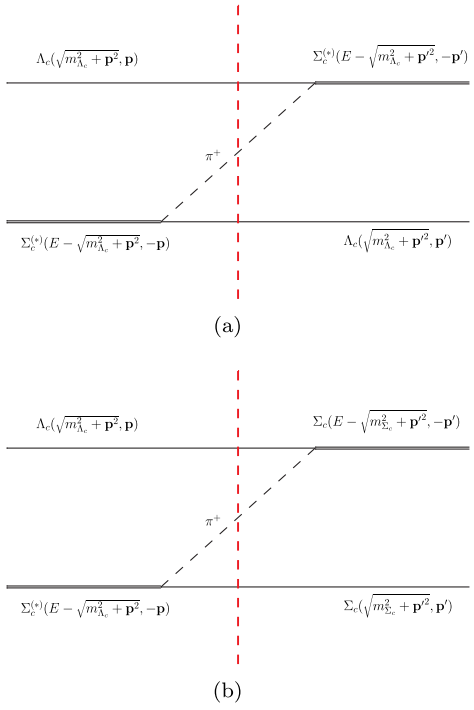

FIG. 2. Three-body intermediate state diagram in the processes (a) $\Lambda_c\Sigma_c^{(*)} \to \Sigma_c^{(*)}\Lambda_c$ and (b) $\Lambda_c\Sigma_c^{(*)} \to \Sigma_c\Sigma_c$. We assume the total energy is E, and the baryons cut by the red dashed line are on shell.

We will neglect the kinetic energy terms $\boldsymbol{p}^2/2m_{\Lambda_c}$ and $\boldsymbol{p}'^2/2m_{\Lambda_c}$ of the charmed baryons due to the heavy quark approximation. Then, we make an energy shift $E \to E + 2m_{\Lambda_c}$, and q_0 gives $q_0 = E + m_{\Sigma_c} - m_{\Lambda_c}$. For the process containing the $\Sigma_c\Sigma_c$ channel, we take $q_0 = 0$ in the diagonal process $\Sigma_c\Sigma_c \to \Sigma_c\Sigma_c$ and $q_0 = E$ in the nondiagonal process $\Lambda_c\Sigma_c^{(*)} \to \Sigma_c\Sigma_c$. We illustrate the latter one in Fig. 2(b). In this work, the latter one could also provide an imaginary part when the energy is around the threshold of $\Sigma_c\Sigma_c$. In fact, we also use these assumptions in the process with other propagators. We list q_0 values for different cases in Table III. To distinguish the special q_0 in the cross diagrams $\Lambda_c\Sigma_c^{(*)} \to \Sigma_c^{(*)}\Lambda_c$ from q_0 in the direct diagrams $\Lambda_c\Sigma_c^{(*)} \to \Lambda_c\Sigma_c^{(*)}$, we use the shorthand "$q_0^C$" for the former cases when we give concrete expressions of the potentials.

TABLE III. The q_0 is the zeroth component of the transferred momentum. E is the total energy relative to the threshold of $\Lambda_c\Sigma_c$. $q_0 = E + m_{\Sigma_c} - m_{\Lambda_c}$ is from the cross diagram $\Lambda_c\Sigma_c^{(*)} \to \Sigma_c^{(*)}\Lambda_c$, and q_0 from the direct diagram $\Lambda_c\Sigma_c^{(*)} \to \Lambda_c\Sigma_c^{(*)}$ is equal to 0. The cases not listed all give $q_0 = 0$.

Process	$\Lambda_c\Sigma_c^{(*)} \to \Sigma_c^{(*)}\Lambda_c$	$\Lambda_c\Sigma_c^{(*)} \to \Sigma_c\Sigma_c$
q_0	$E + m_{\Sigma_c} - m_{\Lambda_c}$	E
Process	$\Lambda_c\bar{\Sigma}_c^{(*)} \to \Sigma_c^{(*)}\bar{\Lambda}_c$	$\Lambda_c\bar{\Sigma}_c^{(*)} \to \Sigma_c\bar{\Sigma}_c$
q_0	$E + m_{\Sigma_c} - m_{\Lambda_c}$	E

III. LAGRANGIANS AND POTENTIALS

The effective Lagrangians are built under the heavy quark symmetry and SU(3)-flavor symmetry. The concrete expressions of the OBE Lagrangians read as

$$\mathcal{L}_B = \mathcal{L}_{B_{\bar{3}}} + \mathcal{L}_S + \mathcal{L}_{\rm int}, \tag{6}$$

$$\begin{aligned}
\mathcal{L}_{B_{\bar{3}}} &= \frac{1}{2}\langle \bar{B}_{\bar{3}}(iv\cdot D)B_{\bar{3}}\rangle + i\beta_B\langle \bar{B}_{\bar{3}}v^\mu(\Gamma_\mu - V_\mu)B_{\bar{3}}\rangle \\
&\quad + l_B\langle \bar{B}_{\bar{3}}\sigma B_{\bar{3}}\rangle, \\
\mathcal{L}_S &= -\langle \bar{S}^\alpha(iv\cdot D - \Delta_B)S_\alpha\rangle + \frac{3}{2}g_1(iv_k)\epsilon^{\mu\nu\lambda\kappa}\langle \bar{S}_\mu \mathbb{A}_\nu S_\lambda\rangle \\
&\quad + i\beta_S\langle \bar{S}_\mu v_\alpha(\Gamma^\alpha - V^\alpha)S_\mu\rangle + \lambda_S\langle \bar{S}_\mu F^{\mu\nu}S_\nu\rangle + l_S\langle \bar{S}_\mu\sigma S_\mu\rangle, \\
\mathcal{L}_{\rm int} &= g_4\langle \bar{S}^\mu \mathbb{A}_\mu B_{\bar{3}}\rangle + i\lambda_I\epsilon^{\mu\nu\lambda\kappa}v_\mu\langle \bar{S}_\nu F^{\lambda\kappa}B_{\bar{3}}\rangle + \text{H.c.}
\end{aligned}$$

S^μ and $B_{\bar{3}}$ are the heavy sextet and antitriplet baryon superfield defined as

$$S_\mu = B_\mu^* - \frac{1}{\sqrt{3}}(\gamma_\mu + v_\mu)\gamma^5 B_6. \tag{7}$$

These heavy baryon fields are

$$\begin{aligned}
B_{\bar{3}} &= \begin{pmatrix} 0 & \Lambda_Q & \Xi_Q^{+1/2} \\ -\Lambda_Q & 0 & \Xi_Q^{-1/2} \\ \Xi_Q^{+1/2} & \Xi_Q^{-1/2} & 0 \end{pmatrix}, \\
B_6 &= \begin{pmatrix} \Sigma_Q^{+1} & \frac{1}{\sqrt{2}}\Sigma_Q^0 & \frac{1}{\sqrt{2}}\Xi_Q'^{+1/2} \\ \frac{1}{\sqrt{2}}\Sigma_Q^0 & \Sigma_Q^{-1} & \frac{1}{\sqrt{2}}\Xi_Q'^{-1/2} \\ \frac{1}{\sqrt{2}}\Xi_Q'^{+1/2} & \frac{1}{\sqrt{2}}\Xi_Q'^{-1/2} & \Omega_Q \end{pmatrix}, \\
B_6^* &= \begin{pmatrix} \Sigma_Q^{*+1} & \frac{1}{\sqrt{2}}\Sigma_Q^{*0} & \frac{1}{\sqrt{2}}\Xi_Q^{*'+1/2} \\ \frac{1}{\sqrt{2}}\Sigma_Q^{*0} & \Sigma_Q^{*-1} & \frac{1}{\sqrt{2}}\Xi_Q^{*'-1/2} \\ \frac{1}{\sqrt{2}}\Xi_Q^{*'+1/2} & \frac{1}{\sqrt{2}}\Xi_Q^{*'-1/2} & \Omega_Q^* \end{pmatrix}.
\end{aligned} \tag{8}$$

The light meson parts are given below

$$\mathbb{A}=\frac{i}{2}[\xi^\dagger(\partial_\mu\xi)+(\partial_\mu\xi)\xi^\dagger],\qquad \Gamma_\mu=\frac{1}{2}[\xi^\dagger(\partial_\mu\xi)-(\partial_\mu\xi)\xi^\dagger],$$
$$F_{\mu\nu}=\partial_\mu V_\nu-\partial_\nu V_\mu+[V_\mu,V_\nu],\qquad \xi=\exp\left[\frac{i\mathcal{M}}{f_\pi}\right], \tag{9}$$

$$\mathcal{M}=\begin{pmatrix}\frac{\pi^0}{\sqrt{2}}+\frac{\eta}{\sqrt{6}} & \pi^+ & K^+\\ \pi^- & \frac{\pi^0}{\sqrt{2}}+\frac{\eta}{\sqrt{6}} & K^0\\ K^- & \bar{K}^0 & -\frac{2}{\sqrt{6}}\eta\end{pmatrix},$$
$$V^\mu=i\frac{g_V}{\sqrt{2}}\begin{pmatrix}\frac{\rho^0}{\sqrt{2}}+\frac{\omega}{\sqrt{2}} & \rho^+ & K^{*+}\\ \rho^- & -\frac{\rho^0}{\sqrt{2}}+\frac{\eta}{\sqrt{2}} & K^{*0}\\ K^{*-} & \bar{K}^{*0} & \phi\end{pmatrix}. \tag{10}$$

For the pion decay constant, we use $f_\pi=132\,\mathrm{MeV}$. With $g_\sigma^q=3.65$ and $g_A^q=0.75$ [72] in the quark model, one obtain $l_B=-g_\sigma^q$, $l_S=-2l_B$, $g_1=\frac{4}{3}g_A^q$, $g_3=\frac{\sqrt{3}}{2}g_1$ and $g_5=-\frac{3}{2}g_1$. As for the other coupling constants, we adopt the values in Ref. [21]:

$$g_2=-0.598,\ g_4=0.999,$$
$$\beta_B g_V=-6.0,\ \beta_S g_V=-2\beta_S g_V$$
$$\lambda_S g_V=19.2\mathrm{GeV}^{-1},\ \lambda_I g_V=-\lambda_S g_V/\sqrt{8}. \tag{11}$$

To get the effective potentials, we add a monopole form factor at each vertex

$$F_i(q)=\frac{\Lambda_i^2-m_i^2}{\Lambda_i^2-q^2}, \tag{12}$$

where i stands for one of the propagators (π, η, σ, ρ, and ω), $q^2=q_0^2-\boldsymbol{q}^2$, and Λ_i and m_i are the cutoff parameter and the mass of the corresponding propagator, respectively. After the Fourier transformation

$$V_i(r)=\frac{1}{(2\pi)^3}\int d\boldsymbol{q}^3 e^{-i\boldsymbol{q}\cdot\boldsymbol{r}}V(\boldsymbol{q})F_i^2(q), \tag{13}$$

we can get the coordinate space potentials

$$\begin{aligned}
V^{\Lambda_c\Sigma_c\to\Lambda_c\Sigma_c}=&-\frac{g_2^2}{f_\pi^2}[S(\boldsymbol{\sigma}_1,\boldsymbol{\sigma}_2)Y_3(\Lambda_\pi,q_0^C,m_\pi,r)+T(\boldsymbol{\sigma}_1,\boldsymbol{\sigma}_2)H_3(\Lambda_\pi,q_0^C,m_\pi,r)]\boldsymbol{\epsilon}_3^\dagger\cdot\boldsymbol{\epsilon}_2-\frac{1}{2}(\beta_B\beta_S g_V^2)Y_0(\Lambda_\omega,q_0,m_\omega,r)\\
&-\frac{1}{3}(\lambda_I g_V)^2[2S(\boldsymbol{\sigma}_1,\boldsymbol{\sigma}_2)Y_3(\Lambda_\rho,q_0^C,m_\rho,r)-T(\boldsymbol{\sigma}_1,\boldsymbol{\sigma}_2)H_3(\Lambda_\rho,q_0^C,m_\rho,r)]\boldsymbol{\epsilon}_3^\dagger\cdot\boldsymbol{\epsilon}_2+2l_Bl_SY_0(\Lambda_\sigma,q_0,m_\sigma,r),\\
V^{\Lambda_c\Sigma_c^*\to\Lambda_c\Sigma_c^*}=&-\frac{g_4^2}{f_\pi^2}[S(\boldsymbol{S}_{t3}^\dagger,\boldsymbol{S}_{t2})Y_3(\Lambda_\pi,q_0^C,m_\pi,r)+T(\boldsymbol{S}_{t3}^\dagger,\boldsymbol{S}_{t2})H_3(\Lambda_\pi,q_0^C,m_\pi,r)]\boldsymbol{\epsilon}_3^\dagger\cdot\boldsymbol{\epsilon}_2+\frac{1}{2}(\beta_B\beta_S g_V^2)Y_0(\Lambda_\omega,q_0,m_\omega,r)\\
&+2(\lambda_I g_V)^2[2S(\boldsymbol{S}_{t3}^\dagger,\boldsymbol{S}_{t2})Y_3(\Lambda_\rho,q_0^C,m_\rho,r)-T(\boldsymbol{S}_{t3}^\dagger,\boldsymbol{S}_{t2})H_3(\Lambda_\rho,q_0^C,m_\rho,r)]\boldsymbol{\epsilon}_3^\dagger\cdot\boldsymbol{\epsilon}_2+2l_Bl_SY_0(\Lambda_\sigma,q_0,m_\sigma,r),\\
V^{\Sigma_c\Sigma_c\to\Sigma_c\Sigma_c}=&\frac{g_1^2}{2f_\pi^2}[S(\boldsymbol{\sigma}_1,\boldsymbol{\sigma}_2)Y_3(\Lambda_\pi,q_0,m_\pi,r)+T(\boldsymbol{\sigma}_1,\boldsymbol{\sigma}_2)H_3(\Lambda_\pi,q_0,m_\pi,r)]\boldsymbol{I}_1\cdot\boldsymbol{I}_2-l_S^2Y_0(\Lambda_\sigma,q_0,m_\sigma,r)\\
&+\frac{1}{3}\frac{g_1^2}{2f_\pi^2}[S(\boldsymbol{\sigma}_1,\boldsymbol{\sigma}_2)Y_3(\Lambda_\eta,q_0,m_\eta,r)+T(\boldsymbol{\sigma}_1,\boldsymbol{\sigma}_2)H_3(\Lambda_\eta,q_0,m_\eta,r)]+\frac{1}{2}(g_Sg_V)^2Y_0(\Lambda_\rho,q_0,m_\rho,r)\boldsymbol{I}_1\cdot\boldsymbol{I}_2\\
&-\frac{1}{3}(\lambda_S g_V)^2[2S(\boldsymbol{\sigma}_1,\boldsymbol{\sigma}_2)Y_3(\Lambda_\rho,q_0,m_\rho,r)-T(\boldsymbol{\sigma}_1,\boldsymbol{\sigma}_2)H_3(\Lambda_\rho,q_0,m_\rho,r)]\boldsymbol{I}_1\cdot\boldsymbol{I}_2\\
&+\frac{1}{2}(\beta_S g_V)^2Y_0(\Lambda_\omega,q_0,m_\omega,r)-\frac{1}{3}(\lambda_S g_V)^2[2S(\boldsymbol{\sigma}_1,\boldsymbol{\sigma}_2)Y_3(\Lambda_\omega,q_0,m_\omega,r)-T(\boldsymbol{\sigma}_1,\boldsymbol{\sigma}_2)H_3(\Lambda_\omega,q_0,m_\omega,r)],
\end{aligned} \tag{14}$$

$$\begin{aligned}
V^{\Lambda_c\Sigma_c\to\Lambda_c\Sigma_c^*}=&-\frac{g_2g_4}{f_\pi^2}[S(\boldsymbol{S}_{t3}^\dagger,\boldsymbol{\sigma}_2)Y_3(\Lambda_\pi,q_0^C,m_\pi,r)+T(\boldsymbol{S}_{t3}^\dagger,\boldsymbol{\sigma}_2)H_3(\Lambda_\pi,q_0^C,m_\pi,r)]\boldsymbol{\epsilon}_3^\dagger\cdot\boldsymbol{\epsilon}_2\\
&+\frac{2}{\sqrt{3}}(\lambda_I g_V)^2[2S(\boldsymbol{S}_{t3}^\dagger,\boldsymbol{\sigma}_2)Y_3(\Lambda_\rho,q_0^C,m_\rho,r)-T(\boldsymbol{S}_{t3}^\dagger,\boldsymbol{\sigma}_2)H_3(\Lambda_\rho,q_0^C,m_\rho,r)]\boldsymbol{\epsilon}_3^\dagger\cdot\boldsymbol{\epsilon}_2,\\
V^{\Lambda_c\Sigma_c\to\Sigma_c\Sigma_c}=&\frac{g_1g_2}{\sqrt{2}f_\pi^2}[S(\boldsymbol{\sigma}_1,\boldsymbol{\sigma}_2)Y_3(\Lambda_\pi,q_0,m_\pi,r)+T(\boldsymbol{\sigma}_1,\boldsymbol{\sigma}_2)H_3(\Lambda_\pi,q_0,m_\pi,r)]\boldsymbol{\epsilon}_3^\dagger\cdot\boldsymbol{I}_2\\
&+\frac{2}{3\sqrt{6}}(\lambda_I\lambda_S g_V^2)[2S(\boldsymbol{\sigma}_1,\boldsymbol{\sigma}_2)Y_3(\Lambda_\rho,q_0,m_\rho,r)-T(\boldsymbol{\sigma}_1^\dagger,\boldsymbol{\sigma}_2)H_3(\Lambda_\rho,q_0,m_\rho,r)]\boldsymbol{\epsilon}_3^\dagger\cdot\boldsymbol{I}_2,
\end{aligned}$$

$$V^{\Lambda_c\Sigma_c^*\to\Sigma_c\Sigma_c} = \frac{g_2 g_3}{\sqrt{2}f_\pi^2}[S(\boldsymbol{\sigma}_1,\boldsymbol{S}_{t2})Y_3(\Lambda_\pi,q_0,m_\pi,r) + T(\boldsymbol{\sigma}_1,\boldsymbol{S}_{t2})H_3(\Lambda_\pi,q_0,m_\pi,r)]\boldsymbol{\epsilon}_3^\dagger\cdot\boldsymbol{I}_2$$
$$-\frac{1}{3\sqrt{2}}(\lambda_I\lambda_S g_V^2)[2S(\boldsymbol{\sigma}_1,\boldsymbol{S}_{t2})Y_3(\Lambda_\rho,q_0,m_\rho,r) - T(\boldsymbol{\sigma}_1,\boldsymbol{S}_{t2})H_3(\Lambda_\rho,q_0,m_\rho,r)]\boldsymbol{\epsilon}_3^\dagger\cdot\boldsymbol{I}_2. \quad (15)$$

We added a factor -1 for the cross-diagram potentials, which contain q_0^C. The factor is from the fermion's position exchange and equal to $(-1)^{s-s_1-s_2+l+i-i_1-i_2+1}$, where $s, s_1, s_2, l, i, i_1, i_2$ are spin, orbit, and isospin numbers. $\boldsymbol{\epsilon}$ and $\boldsymbol{I}$ are the isospin polarization vector and isospin operator, respectively, and the isospin-dependent matrix elements are given in Table IV. $\boldsymbol{S}_t$ and $\boldsymbol{\sigma}$ are the spin transition operator and Pauli operator, respectively. The spin-dependent operators have $S(\boldsymbol{a},\boldsymbol{b}) = \boldsymbol{a}\cdot\boldsymbol{b}$ and $T(\boldsymbol{a},\boldsymbol{b}) = 3(\boldsymbol{a}\cdot\boldsymbol{r})(\boldsymbol{b}\cdot\boldsymbol{r})/r^2 - \boldsymbol{a}\cdot\boldsymbol{b}$, whose matrix elements are given in Table V. The Y_3, H_3 functions and relevant Y, H functions are defined as

$$Y(x) = \frac{e^{-x}}{x}, \qquad H(x) = \left(1+\frac{3}{x}+\frac{3}{x^2}\right)Y(x),$$
$$Y_0(\Lambda,q_0,m,r) = \frac{u}{4\pi}\left[Y(ur) - \frac{\chi}{u}Y(\chi r) - \frac{\beta^2}{2\chi u}e^{-\chi r}\right],$$
$$Y_3(\Lambda,q_0,m,r) = \frac{u^3}{12\pi}\left[Y(ur) - \frac{\chi}{u}Y(\chi r) - \frac{\beta^2\chi}{2u^3}e^{-\chi r}\right],$$
$$H_3(\Lambda,q_0,m,r) = \frac{u^3}{12\pi}\left[H(ur) - \left(\frac{\chi}{u}\right)^3 H(\chi r) - \frac{\beta^2}{2\chi u}\frac{\chi^2}{u^2}Y(\chi r) - \frac{\beta^2}{2\chi u}\frac{\chi^2}{u^2}e^{-\chi r}\right], \quad (16)$$

where

$$u = \mathrm{Sign}[\mathrm{Re}(e^{i\theta}\sqrt{m^2-q_0^2})]\sqrt{m^2-q_0^2},$$
$$\beta = \sqrt{\Lambda^2-m^2}, \qquad \chi = \sqrt{\Lambda^2-q_0^2}. \quad (17)$$

TABLE IV. The isospin-dependent ($I=1$) matrix elements of the operators $\boldsymbol{\epsilon}_3^\dagger\cdot\boldsymbol{\epsilon}_2$, $\boldsymbol{\epsilon}_3^\dagger\cdot\boldsymbol{I}_2$ and $\boldsymbol{I}_1\cdot\boldsymbol{I}_2$.

Δ	$\boldsymbol{\epsilon}_3^\dagger\cdot\boldsymbol{\epsilon}_2$	$\boldsymbol{\epsilon}_3^\dagger\cdot\boldsymbol{I}_2$	$\boldsymbol{I}_1\cdot\boldsymbol{I}_2$
$\langle I=1\vert\Delta\vert I=1\rangle$	1	$-\sqrt{2}$	-1

IV. NUMERICAL RESULTS

A. The OPE potential results for the double-charm hexaquark system

We first introduce the OPE potentials to study the double-charm hexaquark system. For the $1(0^+)$ system, we do not get a bound or resonant state with a reasonable cutoff Λ_π. However, we find a quasibound state in the $1(1^+)$ case, and the results are shown in row "Adopt" of Table VI. One could find this pole has an imaginary part corresponding to $-i\Gamma/2$. We give a brief explanation of the measure $\langle\tilde{\psi}_i|\psi_i\rangle$ herein. $\langle\tilde{\psi}_i|\psi_i\rangle = e^{i\theta}\int_0^\infty\{\psi_i(re^{i\theta})\}^2dr$ is the amplitude corresponding to the ith channel. This measure is similar to the definition of the probabilities of bound states. However, one could find that its value could be complex in Table VI and could not be regarded as a probability. This behavior is from the normalization of the resonance wave function [70,73]. However, the quasibound state herein is special. When the bound energy $B.E. \le -(m_{\Sigma_c} - m_{\Lambda_c} - m_\pi)$, the quasibound state turns into a bound state, and the width from the three-body decay effect vanishes. Then, $\langle\tilde{\psi}_i|\psi_i\rangle$ turns into the probability of the ith channel. Hence, this measure could partly reflect the constituents of this special quasibound state. Furthermore, $\sqrt{\langle r^2\rangle}$ is the root-mean-square radius. Its real part is interpreted as an expectation value, and the imaginary part corresponds to a measure of the uncertainty in observation [74].

To make a comparison, we also give the result under the instantaneous approximation in row "$q_0 = 0$" of Table VI.

TABLE V. The spin-dependent matrix elements.

Δ	$S(\boldsymbol{\sigma}_1^\dagger,\boldsymbol{\sigma}_2)$	$T(\boldsymbol{\sigma}_1^\dagger,\boldsymbol{\sigma}_2)$	$S(\boldsymbol{S}_{t3}^\dagger,\boldsymbol{S}_{t2})$	$T(\boldsymbol{S}_{t3}^\dagger,\boldsymbol{S}_{t2})$	$S(\boldsymbol{S}_{t3}^\dagger,\boldsymbol{\sigma}_2)$	$T(\boldsymbol{S}_{t3}^\dagger,\boldsymbol{\sigma}_2)$	$S(\boldsymbol{\sigma}_1,\boldsymbol{S}_{t2})$	$T(\boldsymbol{\sigma}_1,\boldsymbol{S}_{t2})$
$\langle^3S_1\vert\Delta\vert^3S_1\rangle$	1	0	$\frac{1}{3}$	0	$-2\sqrt{\frac{2}{3}}$	0	$2\sqrt{\frac{2}{3}}$	0
$\langle^3D_1\vert\Delta\vert^3S_1\rangle$	0	$2\sqrt{2}$	0	$-\frac{5}{3\sqrt{2}}$	0	$\frac{1}{\sqrt{3}}$	0	$-\frac{1}{\sqrt{3}}$
$\langle^3S_1\vert\Delta\vert^3D_1\rangle$	0	$2\sqrt{2}$	0	$-\frac{5}{3\sqrt{2}}$	0	$\frac{1}{\sqrt{3}}$	0	$-\frac{1}{\sqrt{3}}$
$\langle^3D_1\vert\Delta\vert^3D_1\rangle$	1	-2	$\frac{1}{3}$	$\frac{5}{6}$	$-2\sqrt{\frac{2}{3}}$	$-\frac{1}{\sqrt{6}}$	$2\sqrt{\frac{2}{3}}$	$\frac{1}{\sqrt{6}}$
Δ	$S(\boldsymbol{\sigma}_1^\dagger,\boldsymbol{\sigma}_2)$							
$\langle^1S_0\vert\Delta\vert^1S_0\rangle$	-3							

TABLE VI. Solutions for the double-charm hexaquark with $I(J^P) = 1(1^+)$ in the OPE potential case with $\theta = 20°$. The energies are given relative to the threshold of $\Lambda_c\Sigma_c$. $\sqrt{\langle r^2\rangle} = [e^{3i\theta}\int_0^\infty\{\psi(re^{i\theta})\}^2 r^2 dr]^{1/2}$ is the root-mean-square (rms) radius. $\langle\tilde{\psi}_i|\psi_i\rangle = e^{i\theta}\int_0^\infty\{\psi_i(re^{i\theta})\}^2 dr$ is the amplitude corresponding to the ith channel of $\Lambda_c\Sigma_c(^3S_1, ^3D_1)$, $\Lambda_c\Sigma_c^*(^3S_1, ^3D_1)$, $\Sigma_c\Sigma_c(^3S_1, ^3D_1)$. The data of the row Adopt are the results we actually adopt, and q_0 herein is from Table III. The data of row $q_0 = 0$ are from the instantaneous approximation.

	Λ_π (GeV)	1.0	1.05	1.1
Adopt	Energy (MeV)	$-5.61 - 0.43i$	$-13.90 - 0.29i$	$-25.57 - 0.04i$
	$\sqrt{\langle r^2\rangle}$ (fm)	$1.4 - 0.1i$	0.9	0.7
	$\langle\tilde{\psi}_i\|\psi_i\rangle \times 100$	$(70.7 - 1.4i/1.7/23.9$ $+1.3i/0.9/2.5 + 0.1i/0.3)$	$(59.0 - 0.4i/1.2/34.1$ $+0.41.2/4.2/0.3)$	(50.8/0.8/40.8/1.4/6.0/0.3)
$q_0 = 0$	Energy (MeV)	-0.54	-5.64	-16.51
	$\sqrt{\langle r^2\rangle}$ (fm)	4.1	1.3	0.8
	$\langle\tilde{\psi}_i\|\psi_i\rangle \times 100$	(91.4/1.0/6.4/0.3/0.7/0.2)	(71.7/1.2/22.8/0.8/3.1/0.4)	(56.8/0.8/35.4/1.2/5.5/0.3)

In this case, the imaginary part of the OPE potential from the three-body decay effect disappears, and the pole becomes a bound state. Considering the cases in row "Adopt" with $\Lambda_\pi = 1.0$ and row "$q_0 = 0$" with $\Lambda_\pi = 1.05$, we find their values are close to each other, including the energy $\sqrt{\langle r^2\rangle}$ and $\langle\tilde{\psi}_i|\psi_i\rangle$. In fact, we find this conclusion could extend to other similar systems. In other words, the influence of the three-body decay is small. Therefore, we will take $\sqrt{\langle r^2\rangle}$ and $\langle\tilde{\psi}_i|\psi_i\rangle$ as the reference measures when analyzing the size and constituents of the pole state.

In our framework, the width of a quasibound state should not be larger than the value of Σ_c and will decrease as the binding energy becomes deeper. In fact, it does. Taking the case $\Lambda_\pi = 1.0$ GeV as an example, we get a quasibound state whose binding energy and width is -5.61 and 0.86 MeV, respectively, and its dominant constituents are S-wave $\Lambda_c\Sigma_c$ and $\Lambda_c\Sigma_c^*$. In fact, the main channel $\Lambda_c\Sigma_c(^3S_1)$ contributes a repulsive potential, and $\Lambda_c\Sigma_c^*(^3S_1)$ contributes an attractive potential with an imaginary part. Considering only the former channel, one could not get a bound state. However, one could get a quasibound state when adding the attractive potential of channel $\Lambda_c\Sigma_c^*$. Obviously, the coupled-channel effects play an important role in this system. To gain a deeper insight, we will add the other medium- and short-range potentials in the following parts.

B. The OBE potential results for the double-charm hexaquark system

In this part, we further employ the OBE potential to include the short- and medium-range contribution. Before making a calculation, we need to choose the cutoff for the different vertex first. The same cutoff is usually used for all the OBE potentials, like $\Lambda_\pi = \Lambda_\eta = \Lambda_\sigma = \Lambda_\rho = \Lambda_\omega$ (common cutoff). Another possible choice can be found in Refs. [75,76]. The authors adopted $\Lambda_i = m_i + \alpha\Lambda_{\rm QCD}$ (scaled cutoff), where i corresponds to a propagator (π, η, σ, ρ, ω), $\Lambda_{\rm QCD} = 220$ MeV is the scale of QCD, and α is a dimensionless parameter. However, these two choices could both be invalid in this work.

As shown in Table VI, the cutoff in the OPE potential case is close to 1 GeV, and when we add the other potentials from the OBE interaction and adopt the common cutoff, the reasonable value is around $\Lambda_i \approx 0.8$ GeV. Then a problem emerges. Since $m_\rho/m_\omega \approx 0.78$ GeV, their form factors $F_i(q) = (\Lambda_i^2 - m_i^2)/(\Lambda_i^2 - q^2) \to 0$, and then the short-range ρ, ω potentials go to 0. On the other hand, if we adopt the scaled cutoff scheme, the ρ, ω potentials could be much larger than the π potential. It may also be doubtful since the OPE potential should play a more important role than the one-vector-exchange potentials for the state very close to the thresholds. To deal with this problem, we adopt a compromise scheme assuming $\Lambda_i = m_i[1 + \alpha(\Lambda_{\rm QCD}/m_i)^2]$.

Adopting the compromise scheme for the cutoff, we get the results in the OBE potential case for the $1(1^+)$ system in Table VII. We find a quasibound state, and its behavior is just like the situation in the OPE potential case.

We take $\alpha = 2.2$ as an example and show the eigenvalue distribution in the OBE potential case, as shown in Fig. 3. Obviously, the quasibound state pole is located on the first Riemann sheets (physical sheets) corresponding to the $\Lambda_c\Sigma_c$, $\Lambda_c\Sigma_c^*$, and $\Sigma_c\Sigma_c$ channels and the second Riemann sheets (unphysical sheets) corresponding to the $\Lambda_c\Lambda_c\pi$ three-body channel. In Fig. 4, we choose $\theta = 20°$ and plot the real and imaginary parts of its wave function. Obviously, the S-wave $\Lambda_c\Sigma_c$ and $\Lambda_c\Sigma_c^*$ channels dominate the state.

C. The OBE potential results for the hidden-charm hexaquark system

In this part, we discuss the molecule system of the hidden-charm hexaquark with the OBE potential. The relevant potentials are similar to those of the double-charm cases, and they can be connected by making a G parity transformation for the propagators. In other words,

TABLE VII. Solutions for the double-charm hexaquark with $I(J^P) = 1(1^+)$ in the OBE potential case with $\theta = 20°$. The energies are given relative to the threshold of $\Lambda_c\Sigma_c$. $\sqrt{\langle r^2\rangle} = [e^{3i\theta}\int_0^\infty\{\psi(re^{i\theta})\}^2 r^2 dr]^{1/2}$ is the rms radius. $\langle\tilde{\psi}_i|\psi_i\rangle = e^{i\theta}\int_0^\infty\{\psi_i(re^{i\theta})\}^2 dr$ is the amplitude corresponding to the ith channel of $\Lambda_c\Sigma_c(^3S_1, ^3D_1)$, $\Lambda_c\Sigma_c^*(^3S_1, ^3D_1)$, $\Sigma_c\Sigma_c(^3S_1, ^3D_1)$.

α	2.0	2.2	2.4
Energy (MeV)	$-3.98 - 0.31i$	$-14.27 - 0.25i$	-31.06
$\sqrt{\langle r^2\rangle}$ (fm)	$1.7 - 0.1i$	1.0	0.7
$\langle\tilde{\psi}_i\|\psi_i\rangle \times 100$	$(81.6 - 1.5i/1.7/14.8$ $+1.4i/0.5/1.2 + 0.1i/0.2)$	$(66.5 - 0.4i/1.1/28.2$ $+0.4i/0.8/3.1/0.2)$	$(55.5/0.7/37.3/1.1/5.3/0.2)$

$$V^{AB} = (-1)^{G_i} V^{A\bar{B}}, \tag{18}$$

where A, B are the charmed baryons, and G_i is the G parity of the i propagator, as shown in Table VIII.

Considering the multichannel coupling effect, we adopt the channels in Table I for the systems $1^+(0^{--})$, $1^-(0^{-+})$, $1^+(1^{--})$, and $1^-(1^{-+})$. Compared with the double-charm case, the number of the hidden-charm systems doubles for the existence of the C or G parity number. For the $1^-(0^{-+})$ case, we do not find a pole in a reasonable cutoff region. For the positive G parity case $1^+(0^{--})$, we find a quasibound state, and the results are given in Table IX. This system has only one channel, and one may find a clearer width behavior than in the other coupled-channel systems. When $\alpha = 1.5$, we find a quasibound state with the binding energy of -5.37 MeV and the width of 1.72 MeV. Obviously, the width is very close to the upper limit of this pole—the width of Σ_c.

For the vector cases, both the $1^+(1^{--})$ and $1^-(1^{-+})$ systems can form a quasibound state. We first discuss the $1^-(1^{-+})$ system. Similar to the double-charm case $1(1^+)$, the first diagonal S-wave OPE potential $V_\pi^{\{\Lambda_c\bar{\Sigma}_c\}\to\{\Lambda_c\bar{\Sigma}_c\}}$ is repulsive, and the third diagonal S-wave OPE potential $V_\pi^{[\Lambda_c\bar{\Sigma}_c^*]\to[\Lambda_c\bar{\Sigma}_c^*]}$ is attractive. The numerical results of this pole are given in Table X, and the main contributions are from the S-wave channels $\{\Lambda_c\bar{\Sigma}_c\}$ and $[\Lambda_c\bar{\Sigma}_c^*]$. In fact, this quasibound state is very similar to the pole in the double-charm case $1(1^+)$. They have very similar results with the same energy, including the widths, constituents, and sizes. For example, taking $\alpha = 2.03$, we get the binding energy of -4.21 MeV, the width of 0.56 MeV, the rms of $1.7 - 0.1i$ fm and $\langle\tilde{\psi}_i|\psi_i\rangle \times 100 = (83.8 - 1.3i/2.5/13.2 + 1.3i/0.5)$, which are very similar to the results in Table VI with $\alpha = 2.0$.

Then, we consider the $1^+(1^{--})$ case. Contrary to the $1^-(1^{-+})$ case, the first diagonal S-wave OPE potential $V_\pi^{[\Lambda_c\bar{\Sigma}_c]\to[\Lambda_c\bar{\Sigma}_c]}$ is attractive, and the third diagonal S-wave

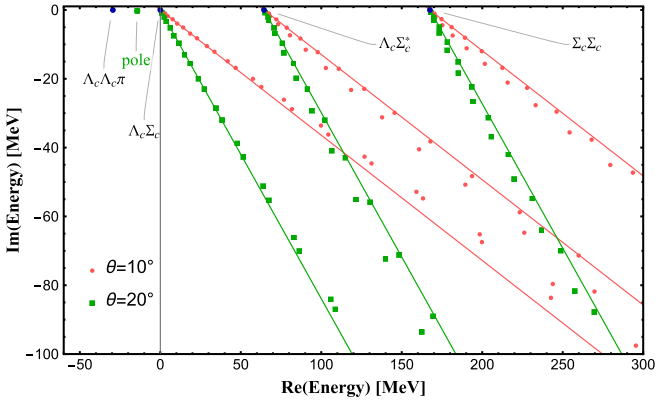

FIG. 3. The eigenvalue distribution of the double-charm hexaquark with $I(J^P) = 1(1^+)$. $\alpha = 2.2$ in the OBE potential case. The red (green) points (square point) and lines correspond to the situation with the complex rotation angle $\theta = 10°(20°)$.

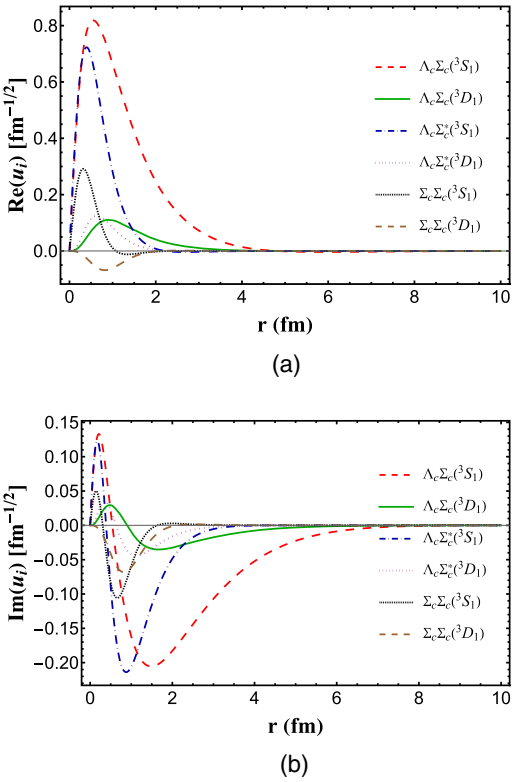

FIG. 4. The wave functions $u_i(r)$ $(i = 1, 2, 3, 4, 5, 6)$ of the double-charm hexaquark with the $I(J^P) = 1(1^+)$. The rotation angle $\theta = 20°$ and the parameter $\alpha = 2.2$ in the OBE potential case. The two diagrams correspond to (a) the real part of $u_i(r)$ and (b) the imaginary part of $u_i(r)$.

TABLE VIII. G parity of the light mesons.

Meson	π	η	σ	ρ	ω
G	-1	1	1	1	-1

TABLE IX. Solutions for the hidden-charm hexaquark with $I^G(J^{PC}) = 1^+(0^{--})$ in the OBE potential case with $\theta = 20°$. The energies are given relative to the threshold of $\Lambda_c\bar{\Sigma}_c$. $\sqrt{\langle r^2\rangle} = [e^{3i\theta}\int_0^\infty\{\psi(re^{i\theta})\}^2r^2dr]^{1/2}$ is the rms radius.

α	1.5	1.8	2.1
Energy (MeV)	$-5.37-0.86i$	$-13.29-0.46i$	$-25.63-0.05i$
$\sqrt{\langle r^2\rangle}$ (fm)	1.7	1.2	0.9

OPE potential $V_\pi^{\Lambda_c\bar{\Sigma}_c^*\to\Lambda_c\bar{\Sigma}_c^*}$ is repulsive. In other words, the first channel can form a bound or quasibound state alone. After considering the coupled-channel effect, we can obtain the solutions, as shown in Table XI. Different from the other cases, this system has two poles when $\alpha \gtrsim 1.8$. The first one is close to the threshold of $\Lambda_c\bar{\Sigma}_c$, and the second to $\Lambda_c\bar{\Sigma}_c^*$. These two poles are quite different.

To study their characters, we illustrate the energy distribution with $\alpha = 1.8$ in Fig. 5. The first pole mainly consists of the S-wave $[\Lambda_c\bar{\Sigma}_c]$ with energy of $-16.79-0.19i$ MeV. It is located on the first Riemann sheets (physical sheets) corresponding to the channels $[\Lambda_c\bar{\Sigma}_c]$, $\{\Lambda_c\bar{\Sigma}_c^*\}$ and $\Sigma_c\bar{\Sigma}_c$, and the second Riemann sheets (unphysical sheets) corresponding to the three-body channel $\Lambda_c\bar{\Lambda}_c\pi$. The second pole mainly consists of the S-wave $\{\Lambda_c\bar{\Sigma}_c^*\}$ with the energy of $60.78-2.03i$ MeV relative to the threshold of $[\Lambda_c\bar{\Sigma}_c]$. It is located on the first Riemann sheets (physical sheets) corresponding to the channels $\{\Lambda_c\bar{\Sigma}_c^*\}$ and $\Sigma_c\bar{\Sigma}_c$, and the second Riemann sheets (unphysical sheets) corresponding to $[\Lambda_c\bar{\Sigma}_c]$ and the $\Lambda_c\bar{\Lambda}_c\pi$ three-body channel. Obviously, the second pole is a Feshbach-type resonance; if we turn off the $\Lambda_c\bar{\Sigma}_c^*$ channels, it disappears. In addition, the width of the first pole is totally from the three-body decay process. However, the width of the second one may have additional sources.

TABLE X. Solutions for the hidden-charm hexaquark with $I^G(J^{PC}) = 1^-(1^{-+})$ in the OBE potential case with $\theta = 20°$. The energies are given relative to the threshold of $\Lambda_c\bar{\Sigma}_c$. $\sqrt{\langle r^2\rangle} = [e^{3i\theta}\int_0^\infty\{\psi(re^{i\theta})\}^2r^2dr]^{1/2}$ is the rms radius. $\langle\tilde{\psi}_i|\psi_i\rangle = e^{i\theta}\int_0^\infty\{\psi_i(re^{i\theta})\}^2dr$ is the amplitude corresponding to the ith channel of $\{\Lambda_c\bar{\Sigma}_c\}(^3S_1, ^3D_1)$, $[\Lambda_c\bar{\Sigma}_c^*](^3S_1, ^3D_1)$.

α	2.1	2.3	2.5
Energy (MeV)	$-6.43-0.32i$	$-15.33-0.23i$	$-27.88-0.01i$
$\sqrt{\langle r^2\rangle}$ (fm)	1.5	1.0	0.8
$\langle\tilde{\psi}_i|\psi_i\rangle\times 100$	$(80.0-1.1i/2.5/17.0+1.1i/0.6)$	$(69.7-0.4i/2.3/27.1+0.4i/0.9)$	$(61.2/2.2/35.4/1.2)$

TABLE XI. Solutions for the hidden-charm hexaquark with $I^G(J^{PC}) = 1^+(1^{--})$ in the OBE potential case with $\theta = 20°$. The energies are given relative to the threshold of $\Lambda_c\bar{\Sigma}_c$. $\sqrt{\langle r^2\rangle} = [e^{3i\theta}\int_0^\infty\{\psi(re^{i\theta})\}^2r^2dr]^{1/2}$ is the rms radius. $\langle\tilde{\psi}_i|\psi_i\rangle = e^{i\theta}\int_0^\infty\{\psi_i(re^{i\theta})\}^2dr$ is the amplitude corresponding to the ith channel of $[\Lambda_c\bar{\Sigma}_c](^3S_1, ^3D_1)$, $\{\Lambda_c\bar{\Sigma}_c^*\}(^3S_1, ^3D_1)$, $\Sigma_c\bar{\Sigma}_c(^3S_1, ^3D_1)$. The data of row "2" are the results we actually adopt, and q_0 herein is from Table III. The data of row "2I" are from the instantaneous approximation with $q_0 = 0$.

Pole	α	1.6	1.8	2.0
1	Energy (MeV)	$-7.21-0.42i$	$-16.79-0.19i$	-32.86
	$\sqrt{\langle r^2\rangle}$ (fm)	1.5	1.1	0.9
	$\langle\tilde{\psi}_i|\psi_i\rangle\times 100$	$(92.2-0.2i/3.4/2.1$ $+0.2/0./0.9/1.5)$	$(88.1/4.3/2.3$ $+0.1i/0./2.5/2.8)$	$(81.5/6.0/$ $1.4/0./6.5/4.6)$
2	Energy (MeV)		$60.78-2.03i$	$41.38-2.66i$
	$\sqrt{\langle r2\rangle}$ (fm)		$1.8-0.3i$	0.8
	$\langle\tilde{\psi}_i|\psi_i\rangle\times 100$		$(-0.4-0.4i/-3.3$ $+4.2i/82.7-10.4i/6.4+1.5i/14.3$ $+4.7i/0.3+0.3i)$	$(1.3+0.5i/5.5+11.9i/55.5$ $-10.3i/0.8-0.6i/36.2$ $-1.8i/0.6+0.2i)$
2I	Energy (MeV)		$60.45-1.73i$	$43.57-2.02i$
	$\sqrt{\langle r2\rangle}$ (fm)		$1.6-0.3i$	0.8
	$\langle\tilde{\psi}_i|\psi_i\rangle\times 100$		$(-0.2+0.4i/-0.5$ $+3.8i/85.6-6.1i/1.4-0.1i/13.6$ $+1.9i/0.1+0.1i)$	$(3.0+0.6i/4.5+7.2i/61.8$ $-8.7i/0.6-0.1i/30.0$ $+1.0i/0.1+0.1i)$

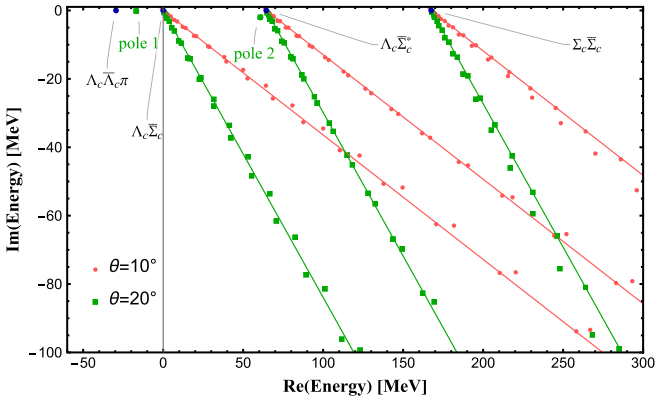

FIG. 5. The eigenvalue distribution of the hidden-charm hexaquark with $I(J^P) = 1^+(1^{--})$. $\alpha = 1.8$ in the OBE potential case. The red (green) points (square point) and lines correspond to the situation with the complex rotation angle $\theta = 10°(20°)$.

To figure out this source, we take the instantaneous approximation $q_0 = 0$. We also obtain two similar poles that correspond to poles "1" and "2" in Table XI. The one corresponding to pole 1 turns into a bound state, and we have discussed this case in Sec. IV A. We will focus on the other pole, whose numerical results are listed in row "2I" of Table XI. Its energy becomes $60.45 - 1.73i$ MeV for the $\alpha = 1.8$ case, whose real part is nearly unchanged compared with the 2 pole with energy of $60.78 - 2.03i$ MeV. However, its width changes and does not disappear like the other quasibound state. As discussed in the Sec. IV A, the width from the three-body decay will vanish under the instantaneous approximation. Therefore, the width in 2I is totally from the two-body decay process, such as the decay of the pole 2I $\to [\Lambda_c\bar{\Sigma}_c]$. We infer from the change of the width that the two-body decay plays a more important role than the three-body decay in this resonance.

Finally, we also plot the wave functions of poles 1 and 2, as shown in Fig. 6. We choose $\theta = 20°$ and present the real and imaginary parts of their wave functions. Obviously, the S-wave $[\Lambda_c\bar{\Sigma}_c]$ and $\{\Lambda_c\bar{\Sigma}_c^*\}$ channels dominate the first pole, and the S-wave $\{\Lambda_c\bar{\Sigma}_c^*\}$ channel dominates the second pole.

V. SUMMARY

In this work, we use the complex scaling method to study the double-charm and hidden-charm hexaquark states in the molecule picture. In order to include the coupled-channel effects, we consider the channels $\Lambda_c\Sigma_c^{(*)}$ (or $\Lambda_c\bar{\Sigma}_c^{(*)}$) and $\Sigma_c\Sigma_c$ (or $\Sigma_c\bar{\Sigma}_c$). We also take into account the $S - D$ wave mixing effect in this deuteronlike dibaryon (hidden-charm baryonium), as shown in Table I.

We adopt the effective Lagrangians constructed in terms of the heavy quark symmetry and chiral symmetry.

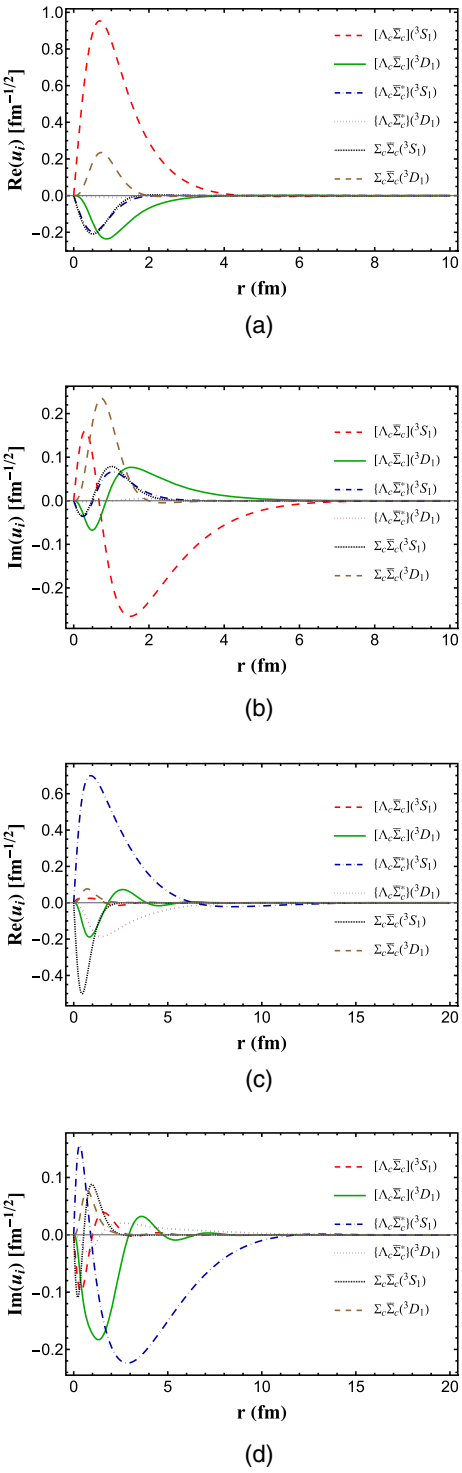

FIG. 6. The wave functions $u_i(r)$ $(i = 1, 2, 3, 4, 5, 6)$ of the hidden-charm hexaquark with $I(J^P) = 1^+(1^{--})$. The rotation angle $\theta = 20°$ and the parameter $\alpha = 1.8$ in the OBE potential case. The four diagrams correspond to (a) the real part of $u_i(r)$ for the first pole, (b) the imaginary part of $u_i(r)$ for the first pole, (c) the real part of $u_i(r)$ for the second pole, and (d) the imaginary part of $u_i(r)$ for the second pole.

To figure out the influence of the long-range pion exchange in the formation of the bound states and resonances, we adopt the OPE potential for the double-charm hexaquark system. We also give the numerical results with the OBE potential for the double-charm and hidden-charm hexaquark systems.

The OPE potentials of $\Lambda_c\Sigma_c^{(*)}$ and the tetraquark DD^* systems are similar. They both have an imaginary part. This imaginary part comes from the processes $\Sigma_c^{(*)} \to \Lambda_c\pi$ ($D^* \to D\pi$), which can be naturally understood in the framework of the CSM. In the study of the double-charm hexaquark system with the OPE potential, we find a quasibound state in the $1(1^+)$ system, which mainly consists of the S-wave $\Lambda_c\Sigma_c$ and $\Lambda_c\Sigma_c^*$. When taking $\Lambda_\pi = 1$ GeV, the binding energy relative to $\Lambda_c\Sigma_c$ is -5.6 MeV, and the width is 0.86 MeV. As explained in Sec. IV A, this width is totally from the $\Lambda_c\Lambda_c\pi$ three-body decay process. For the system with $1(0^+)$, we do not find a bound state or resonance.

We also employ the OBE potential to include the medium- and short-range interactions, and we get a similar result compared with the OPE case—only one pole is found. Its binding energy relative to $\Lambda_c\Sigma_c$ and the width is -14.27 and 0.50 MeV, respectively, when taking $\alpha = 2.2$. The S-wave $\Lambda_c\Sigma_c$ and $\Lambda_c\Sigma_c^*$ are the dominant constituents, and the D-wave constituents still provide small contributions.

For the hidden-charm hexaquark systems, we find more poles. In the $1^-(0^{-+})$ case, we do not find a pole in a reasonable cutoff region. However, we find a quasibound state in the $1^+(0^{--})$ case with a single channel. When $\alpha = 1.5$, the binding energy is -5.37 MeV relative to the $\Lambda_c\bar{\Sigma}_c$ threshold. Its width is 1.72 MeV, which is very close to the width of Σ_c. In the vector cases, we find poles in both the $1^+(1^{--})$ and $1^-(1^{-+})$ cases. For the $1^-(1^{-+})$ case, we find a quasibound state, which behaves just like the mentioned pole in the $1(1^+)$ double-charm hexaquark. We get this pole in a similar region $\alpha \in [2.0 \sim 2.5]$. For the same energy or cutoff, their widths, sizes, and constituents are close to each other too. For the $1^+(1^{--})$ case, we find two poles—a pole close to the $\Lambda_c\bar{\Sigma}_c$ threshold and the other close to the $\Lambda_c\bar{\Sigma}_c^*$ threshold. Taking $\alpha = 1.8$, the first pole as a quasibound state has a binding energy of -16.79 MeV and a width of 0.38 MeV, and the S-wave $[\Lambda_c\bar{\Sigma}_c]$ plays a dominant role. The second pole is a resonance, whose energy relative to the $\Lambda_c\bar{\Sigma}_c$ threshold is $60.78-2.03i$ MeV. Different from the above quasibound states whose widths are totally from the three-body decay, its width arises from two sources—the three-body decay and the two-body decay. As shown in Table XI, its width does not vanish when we get rid of the three-body decay effect, and the contribution from the two-body decay is apparently larger. We also plot the wave functions of these two poles; see in Fig. 6.

In principle, the annihilation channels may also contribute to the decay widths of the hidden-charm hexaquark states. The neglect of the annihilation is responsible for the failure of the quasinuclear approach to the baryonium which predicted several narrow $N\bar{N}$ states that have not been observed so far [77–79]. For the vector charmonium, the suppression of the annihilation decays results from the Zweig rule where the color-singlet $c\bar{c}$ pair can only annihilate into three gluons due to the charge parity conservation. This is seemingly not the case for the $c\bar{c}$ pair within a baryon-antibaryon wave function. In the present work, we are mainly interested in the near-threshold states which are either loosely bound states or resonances with a relatively large radius around 1–2 fm. In other words, the charmed baryon and antibaryon are well separated from each other, while the annihilation of the $c\bar{c}$ pair occurs at very short distance, hence, is strongly suppressed. Such a suppression is observed in the hidden-charm pentaquark states P_c and tetraquark states Z_c. For example, the dominant decay modes of $Z_c(3900)$ are the open-charm modes $D\bar{D}^*$, while the hidden-charm modes $J/\psi\pi$, etc., are also important. None of the annihilation channels has been observed up to now.

In summary, we find some quasibound states and resonances in these systems. One could look for these states through their strong decay patterns, such as $[\Lambda_c\bar{\Sigma}_c]$ and $\Lambda_c\bar{\Lambda}_c\pi$ invariant mass distributions in the hidden-charm baryonium and $\Lambda_c\Lambda_c\pi$ invariant mass distribution in the double-charm dibaryon. In particular, the $1^+(0^{--})$ and $1^-(1^{-+})$ hidden-charm hexaquark molecular states are very interesting. These isovector mesons have exotic J^{PC} quantum numbers which are not accessible to the conventional $q\bar{q}$ mesons. Hopefully, this work can be helpful for future experimental search of the hexaquark states at facilities such as LHCb and Belle II.

ACKNOWLEDGMENTS

This research is supported by the National Science Foundation of China under Grants No. 11975033, No. 12070131001, and No. 12147168. The authors thank K. Chen for helpful discussions.

[1] P. Adlarson *et al.*, Phys. Rev. Lett. **106**, 242302 (2011).
[2] P. Adlarson *et al.*, Phys. Lett. B **721**, 229 (2013).
[3] P. Adlarson *et al.*, Phys. Rev. C **88**, 055208 (2013).
[4] P. Adlarson *et al.*, Phys. Rev. Lett. **112**, 202301 (2014).
[5] M. Bashkanov *et al.*, Phys. Rev. Lett. **102**, 052301 (2009).
[6] R. L. Jaffe, Phys. Rev. Lett. **38**, 195 (1977).
[7] K.-W. Li, T. Hyodo, and L.-S. Geng, Phys. Rev. C **98**, 065203 (2018).
[8] K. Morita, T. Furumoto, and A. Ohnishi, Phys. Rev. C **91**, 024916 (2015).
[9] T. Inoue, N. Ishii, S. Aoki, T. Doi, T. Hatsuda, Y. Ikeda, K. Murano, H. Nemura, and K. Sasaki, Phys. Rev. Lett. **106**, 162002 (2011).
[10] S. R. Beane *et al.*, Phys. Rev. Lett. **106**, 162001 (2011).
[11] C. J. Yoon *et al.*, Phys. Rev. C **75**, 022201 (2007).
[12] H. Polinder, J. Haidenbauer, and U.-G. Meißner, Phys. Lett. B **653**, 29 (2007).
[13] H. Takahashi *et al.*, Phys. Rev. Lett. **87**, 212502 (2001).
[14] S. D. Paganis, G. W. Hoffmann, R. L. Ray, J.-L. Tang, T. Udagawa, and R. S. Longacre, Phys. Rev. C **62**, 024906 (2000).
[15] G. Karl and P. Zenczykowski, Phys. Rev. D **36**, 2079 (1987).
[16] J. L. Rosner, Phys. Rev. D **33**, 2043 (1986).
[17] S. A. Yost and C. R. Nappi, Phys. Rev. D **32**, 816 (1985).
[18] P. B. Mackenzie and H. B. Thacker, Phys. Rev. Lett. **55**, 2539 (1985).
[19] A. P. Balachandran, A. Barducci, F. Lizzi, V. G. J. Rodgers, and A. Stern, Phys. Rev. Lett. **52**, 887 (1984).
[20] F. Frömel, B. Juliá-Díaz, and D. Riska, Nucl. Phys. **A750**, 337 (2005).
[21] Y.-R. Liu and M. Oka, Phys. Rev. D **85**, 014015 (2012).
[22] H. Huang, J. Ping, and F. Wang, Phys. Rev. C **87**, 034002 (2013).
[23] R. Aaij *et al.*, Phys. Rev. Lett. **119**, 112001 (2017).
[24] S.-Q. Luo, K. Chen, X. Liu, Y.-R. Liu, and S.-L. Zhu, Eur. Phys. J. C **77**, 709 (2017).
[25] T. Mehen, Phys. Rev. D **96**, 094028 (2017).
[26] C. E. Fontoura, G. Krein, A. Valcarce, and J. Vijande, Phys. Rev. D **99**, 094037 (2019).
[27] H. Xu, B. Wang, Z.-W. Liu, and X. Liu, Phys. Rev. D **99**, 014027 (2019).
[28] A. Francis, R. J. Hudspith, R. Lewis, and K. Maltman, Phys. Rev. D **99**, 054505 (2019).
[29] S. S. Agaev, K. Azizi, and H. Sundu, Phys. Rev. D **99**, 114016 (2019).
[30] Y. Tan, W. Lu, and J. Ping, Eur. Phys. J. Plus **135**, 716 (2020).
[31] G. Yang, J. Ping, and J. Segovia, Phys. Rev. D **101**, 014001 (2020).
[32] J.-B. Cheng, S.-Y. Li, Y.-R. Liu, Z.-G. Si, and T. Yao, Chin. Phys. C **45**, 043102 (2021).
[33] Q. Qin, Y.-F. Shen, and F.-S. Yu, Chin. Phys. C **45**, 103106 (2021).
[34] R. Aaij *et al.*, Nat. Phys. **18**, 751 (2022).
[35] R. Aaij *et al.*, Nat. Commun. **13**, 3351 (2022).
[36] T. F. Caramés and A. Valcarce, Phys. Rev. D **92**, 034015 (2015).
[37] H. Garcilazo and A. Valcarce, Eur. Phys. J. C **80**, 720 (2020).
[38] H. Huang, J. Ping, and F. Wang, Phys. Rev. C **89**, 035201 (2014).
[39] Z. Xia, S. Fan, X. Zhu, H. Huang, and J. Ping, Phys. Rev. C **105**, 025201 (2022).
[40] Zhe Liu, Hong-Tao An, Zhan-Wei Liu, and Xiang Liu, arXiv:2209.10440.
[41] X.-W. Wang, Z.-G. Wang, and G.-L. Yu, Eur. Phys. J. A **57**, 275 (2021).
[42] Kan Chen, Bo-Lin Huang, Bo Wang, and Shi-Lin Zhu, arXiv:2204.13316.
[43] J.-X. Lu, L.-S. Geng, and M. P. Valderrama, Phys. Rev. D **99**, 074026 (2019).
[44] R. Chen, A. Hosaka, and X. Liu, Phys. Rev. D **96**, 116012 (2017).
[45] N. Lee, Z.-G. Luo, X.-L. Chen, and S.-L. Zhu, Phys. Rev. D **84**, 014031 (2011).
[46] N. Li and S.-L. Zhu, Phys. Rev. D **86**, 014020 (2012).
[47] X.-Z. Ling, M.-Z. Liu, and L.-S. Geng, Eur. Phys. J. C **81**, 1090 (2021).
[48] W. Meguro, Y.-R. Liu, and M. Oka, Phys. Lett. B **704**, 547 (2011).
[49] L. Meng, N. Li, and S.-L. Zhu, Eur. Phys. J. A **54**, 143 (2018).
[50] Z. Yu, M. Song, J.-Y. Guo, Y. Zhang, and G. Li, Phys. Rev. C **104**, 035201 (2021).
[51] J. Vijande, A. Valcarce, J.-M. Richard, and P. Sorba, Phys. Rev. D **94**, 034038 (2016).
[52] X.-K. Dong, F.-K. Guo, and B.-S. Zou, Commun. Theor. Phys. **73**, 125201 (2021).
[53] S. M. Gerasyuta and E. E. Matskevich, Int. J. Mod. Phys. E **21**, 1250058 (2012).
[54] Z. Liu, H.-T. An, Z.-W. Liu, and X. Liu, Phys. Rev. D **105**, 034006 (2022).
[55] Y.-D. Chen and C.-F. Qiao, Phys. Rev. D **85**, 034034 (2012).
[56] Y.-D. Chen, C.-F. Qiao, P.-N. Shen, and Z.-Q. Zeng, Phys. Rev. D **88**, 114007 (2013).
[57] H.-X. Chen, D. Zhou, W. Chen, X. Liu, and S.-L. Zhu, Eur. Phys. J. C **76**, 602 (2016).
[58] C.-F. Qiao, Phys. Lett. B **639**, 263 (2006).
[59] C.-F. Qiao, J. Phys. G **35**, 075008 (2008).
[60] B.-D. Wan, L. Tang, and C.-F. Qiao, Eur. Phys. J. C **80**, 121 (2020).
[61] J.-B. Cheng, Z.-Y. Lin, and S.-L. Zhu, Phys. Rev. D **106**, 016012 (2022).
[62] Zi-Yang Lin, Jian-Bo Cheng, and Shi-Lin Zhu, arXiv:2205.14628.
[63] J. Aguilar and J. M. Combes, Commun. Math. Phys. **22**, 269 (1971).
[64] E. Balslev and J. M. Combes, Commun. Math. Phys. **22**, 280 (1971).
[65] P. A. Zyla *et al.* (Particle Data Group), Prog. Theor. Exp. Phys. **2020**, 083C01 (2020).
[66] S. Aoyama, T. Myo, K. Katō, and K. Ikeda, Prog. Theor. Phys. **116**, 1 (2006).
[67] Y. Ho, Phys. Rep. **99**, 1 (1983).
[68] E. Hiyama, Y. Kino, and M. Kamimura, Prog. Part. Nucl. Phys. **51**, 223 (2003).
[69] T. Noro and H. S. Taylor, J. Phys. B **13**, L377 (1980).
[70] T. N. Rescigno and C. W. McCurdy, Phys. Rev. A **34**, 1882 (1986).

[71] J. J. Wendoloski and W. P. Reinhardt, Phys. Rev. A **17**, 195 (1978).
[72] A. Manohar and H. Georgi, Nucl. Phys. **B234**, 189 (1984).
[73] R. M. More and E. Gerjuoy, Phys. Rev. A **7**, 1288 (1973).
[74] M. Homma, T. Myo, and K. Kato, Prog. Theor. Phys. **97**, 561 (1997).
[75] H.-Y. Cheng, C.-K. Chua, and A. Soni, Phys. Rev. D **71**, 014030 (2005).
[76] Y.-R. Liu and M. Oka, Phys. Rev. D **85**, 014015 (2012).
[77] E. Fermi and C. N. Yang, Phys. Rev. **76**, 1739 (1949).
[78] C. B. Dover, S. H. Kahana, and T. L. Trueman, Phys. Rev. D **16**, 799 (1977).
[79] C. B. Dover and M. Goldhaber, Phys. Rev. D **15**, 1997 (1977).